Spectrum of Engineering Sciences
ISSN (e) 3007-3138 **(p)** 3007-312X
Volume 4, Issue 6, 2026

ENHANCING WAVE ENERGY EXTRACTION THROUGH BUOY GEOMETRY OPTIMIZATION: COMPARATIVE ANALYSIS AND EXPERIMENTAL VALIDATION OF A CYLINDRICAL–SPHERICAL POINT ABSORBER

Basit Ali Wajid[*1], Muhammad Lolak[2], Muhammad Haseeb[3], Muhammad Asad Randhawa[4], Muhammad Haider Ali[5]

[*1,2,3,4,5]*Department of Mechanical Engineering, University of Engineering and Technology Lahore*

DOI: https://doi.org/10.5281/zenodo.20823284

Keywords
Wave energy converter; Point absorber; Buoy geometry optimization; Hydrodynamic analysis; ANSYS AQWA; Response amplitude operator; Radiation damping; Rack-and-pinion power take-off; Froude scaling

Article History
Received: 26 April 2026
Accepted: 08 June 2026
Published: 24 June 2026

Corresponding Author: *
Basit Ali Wajid

Abstract

The commercial viability of point absorber wave energy converters (PA-WECs) remains constrained by the strong sensitivity of energy capture to floater geometry, yet direct comparative assessments of dissimilar buoy shapes under a unified numerical framework are scarce in the literature. This study presents a combined computational fluid dynamics (CFD) and frequency-domain hydrodynamic investigation of three candidate point absorber geometries a multi-section optimized buoy, a top-shaped buoy, and a cylindrical–spherical buoy developed in SolidWorks and evaluated under identical regular wave conditions. Volume-of-fluid (VOF) simulations with the SST k–ω closure were performed in ANSYS Fluent to characterize near-field velocity and pressure loading, while boundary element method (BEM) computations in ANSYS AQWA quantified added mass, radiation damping, wave excitation, response amplitude operator (RAO), and heave response. The CFD results revealed nearly indistinguishable flow fields (peak velocities of 1.65–1.69 m/s; peak pressures of 14.65–14.69 kPa), demonstrating that near-field loading alone cannot discriminate geometric performance. In contrast, the frequency-domain analysis exposed pronounced differences: the cylindrical–spherical buoy achieved the highest added mass (2.31 kg at 7.62 rad/s) and radiation damping (17.57 N/(m/s) at 11.72 rad/s) 4.9 and 6.5 times those of the top-shaped buoy, respectively together with the largest displaced volume (2.78×10^{-3} m^3). Although the multi-section buoy produced the largest heave RAO (5.66 m/m at 6.08 rad/s), the superior radiative coupling of the cylindrical–spherical buoy yielded the greatest power absorption capacity, with a theoretical mechanical absorption of 6.40 W and electrical output of 5.12 W at a wave amplitude of 0.025 m and frequency of 7.854 rad/s. A 0.574-scale prototype integrating a rack-and-pinion power take-off (PTO) and a DC generator was fabricated and tested in a 914 × 457 × 610 mm acrylic wave flume, generating peak voltages up to 1.50 V. Froude-type scaling ($P \propto \lambda^{3.5}$) reconciled the measured output with the numerical predictions, confirming that the discrepancy between the full-model estimate and the prototype response is dominated by geometric scale rather than modeling error. The results establish that maximizing radiative coupling and displaced volume rather than raw motion amplitude governs PTO-based energy extraction and identify the cylindrical–

spherical buoy as the optimal configuration for small-scale wave energy harvesting applications.

1. INTRODUCTION

The accelerating global demand for electricity, coupled with the environmental burden of fossil-fuel-dominated generation, has intensified the search for renewable resources capable of delivering dense, predictable, and continuously available power [1], [2]. Among marine renewable resources, ocean wave energy occupies a distinctive position: its theoretical global potential is estimated at several terawatts [3], its power density exceeds that of solar and wind by one to two orders of magnitude, and its short-term predictability sea states can be forecast days in advance renders it particularly attractive for grid integration and for powering remote offshore infrastructure such as navigation aids, aquaculture facilities, and oceanographic monitoring buoys [4], [5].

The increasing demand for sustainable energy solutions has accelerated research efforts in diverse yet interconnected domains, including Zero Energy Buildings (ZEBs) [6], [7], [8], nano-energy harvesting technologies [9], vibration signal processing and active control methodologies [10], [11], and emission control systems [12]. These technologies play a crucial role in maximizing energy utilization, minimizing energy losses, reducing greenhouse gas emissions, and enabling the efficient conversion of otherwise wasted ambient energy into usable electrical power. Consequently, their integration has emerged as a key strategy for addressing global energy challenges while promoting environmentally sustainable and energy-efficient engineering infrastructures.

A broad family of wave energy converter (WEC) architectures has been proposed to harvest this resource, conventionally classified into oscillating water columns, overtopping devices, and oscillating body systems [13], [14]. Within the oscillating body class, point absorber wave energy converters (PA-WECs) compact floaters whose horizontal dimensions are small relative to the incident wavelength have attracted sustained research attention owing to their scalability, omnidirectional energy capture, ease of deployment, and mechanical simplicity [15], [16]. In a heave-mode PA-WEC, the vertical oscillation of the buoy is transmitted to a power take-off (PTO) mechanism that converts reciprocating motion into rotation and, ultimately, electricity. The complete energy conversion chain adopted in the present study from incident wave to stored electrical energy is illustrated in **Figure 1**.

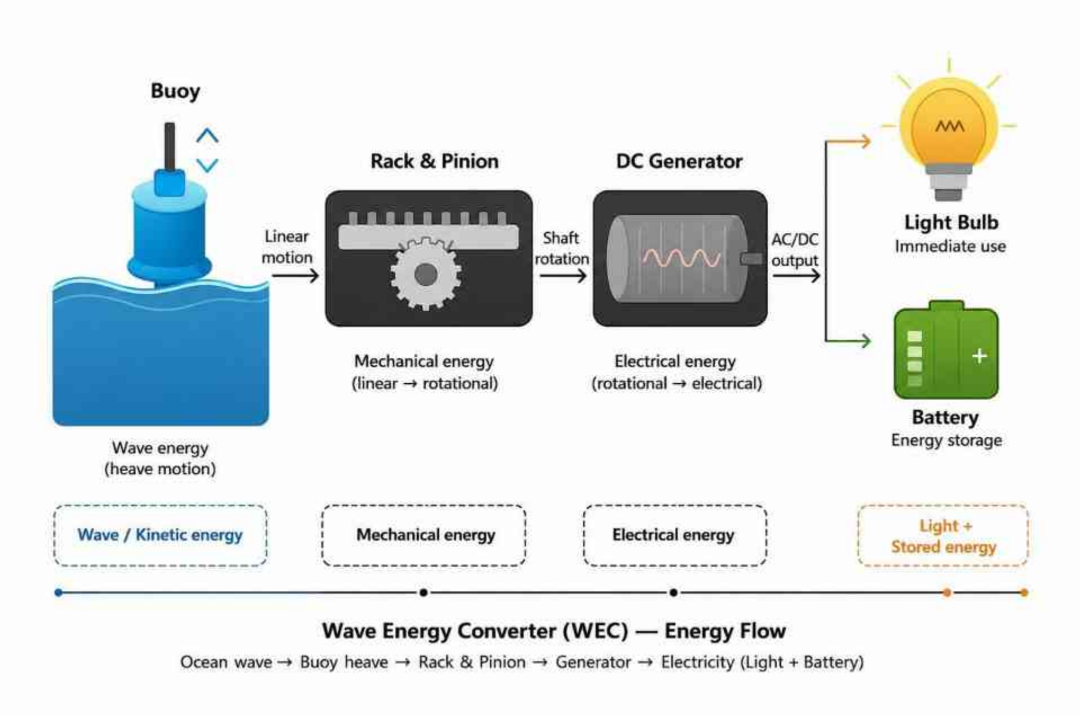

Figure 1: Energy Conversion Chain of the Wave Energy Converter

It is now well established that the hydrodynamic performance of a PA-WEC is governed primarily by the geometry of its floater. The buoy shape dictates the wetted surface over which incident wave pressure acts, the submerged volume that determines hydrostatic stiffness and excitation loading, and the manner in which the oscillating body radiates secondary waves and hence the added mass and radiation damping coefficients that control its resonant behaviour [17], [18]. Azam et al [19]. demonstrated that a spinning top-shaped buoy tailored for low-energy-density seas substantially modified the heave RAO and excitation characteristics relative to conventional cylinders and subsequently extended the concept to a self-stabilizing PA-WEC with a nonlinear PTO for oceanographic applications [20]. Ahmed et al. [21], [22]introduced S-shaped floaters for Wavestar-like converters and showed that profile curvature materially alters the hydrodynamic coefficients and capture efficiency, while their later isomorphic Froude scaling study of bulbous-bottomed buoys [23] highlighted the decisive role of submerged volume distribution in tuning resonance. Complementary geometric optimization studies by Gao and Xiao [17], Pastor and Liu [24], Shadman et al. [25], Guo and Ringwood [18], and Garcia-Teruel and Forehand [26] have collectively confirmed that floater shape is the single most influential passive design variable in point absorber performance.

Notwithstanding this progress, three limitations persist in the available literature. First, the majority of geometric investigations examine a single buoy concept in isolation top-shaped [19], S-shaped [21], or bulbous-bottomed [23] under study-specific wave climates, numerical settings, and mass properties, which precludes direct cross-comparison of dissimilar shapes. Second, most studies rely on either potential-flow (BEM) hydrodynamics or viscous CFD but rarely combine both within a single framework; consequently, the complementary information contained in near-field viscous loading and in frequency-domain radiation/diffraction coefficients is seldom exploited jointly. Third, buoy selection is frequently based on motion amplitude (RAO) alone, although for PTO-coupled converters the extractable power is governed by the product of radiation damping and the square of heave velocity, so that the buoy with the largest motion is not necessarily the buoy that delivers the most energy.

The present work addresses these gaps through a unified comparative investigation of three-point absorber buoy geometries a multi-section optimized buoy (Buoy 1), a top-shaped buoy (Buoy 2), and a cylindrical–spherical buoy (Buoy 3) evaluated under strictly identical numerical wave conditions. The novel contributions of this study are fourfold: (1) a dual-framework comparison methodology combining transient VOF CFD simulations (ANSYS Fluent) with frequency-domain BEM hydrodynamics (ANSYS AQWA) for three dissimilar buoy shapes under identical environmental and mass conditions; (2) an absorption-oriented selection criterion demonstrating, with quantitative evidence, that radiative coupling and displaced volume rather than peak RAO should govern buoy selection for PTO-based converters; (3) end-to-end power estimation propagating the AQWA hydrodynamic coefficients through a radiation-damping-based absorption model to predict mechanical (6.40 W) and electrical (5.12 W) outputs for the optimal geometry; and (4) experimental validation with explicit scaling reconciliation, in which a 0.574-scale prototype with a rack-and-pinion PTO and DC generator is tested in a laboratory wave flume and the measured output is reconciled with numerical predictions through Froude-type power scaling ($P \propto \lambda^{3.5}$).

The specific objectives of the study are: (i) to develop three-dimensional CAD models of the candidate buoys in SolidWorks; (ii) to characterize the near-field flow and pressure loading of each buoy using VOF CFD; (iii) to quantify added mass, radiation damping, excitation force, RAO, and heave response using frequency-domain BEM analysis; (iv) to identify the geometry maximizing wave energy absorption; (v) to estimate its power generation capability; and (vi) to validate the concept experimentally through prototype fabrication and wave-flume testing.

2. Methodology

The overall research framework spanning literature review, geometry selection, CAD modeling, parallel CFD and hydrodynamic analyses, comparative assessment, optimal buoy selection, and prototype fabrication is summarized in **Figure 2**.

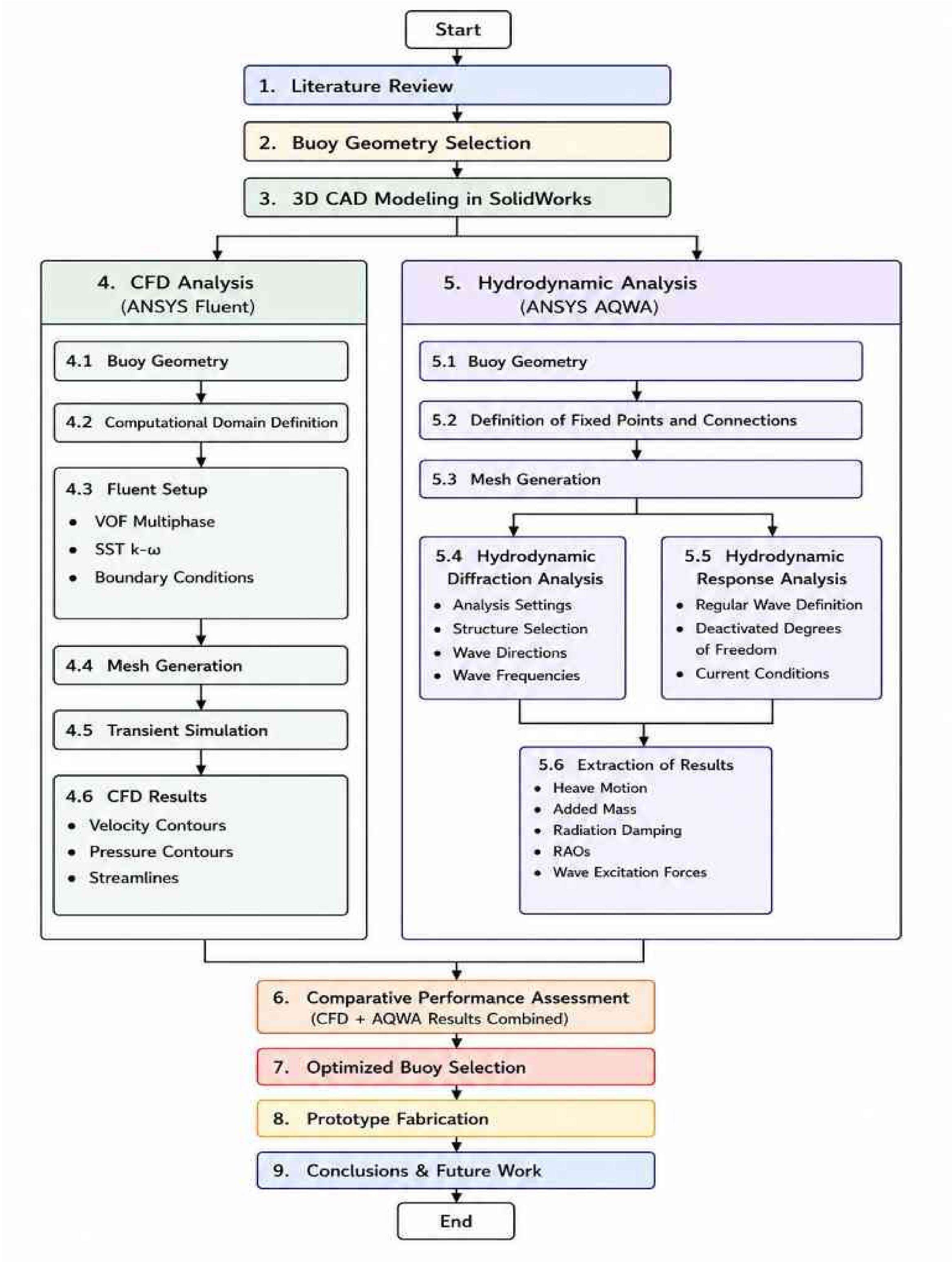

Figure 2: Research Framework Adopted for the Development and Evaluation of the Wave Energy Converter

2.1 Buoy Geometry Development

Three candidate point absorber geometries were developed in SolidWorks on the basis of design concepts established in the recent literature [19]-[23], with the deliberate intention of spanning three distinct hydrodynamic philosophies as shown in **Figure 3**:

Multi-section Optimized Buoy 1. A vertically stacked configuration combining cylindrical and tapered segments with a maximum diameter of 230 mm, a mid-section diameter of 130 mm, and a hemispherical lower closure of radius 45 mm, with a 3 mm wall thickness. The stepped profile is intended to amplify excitation loading by presenting multiple diameter transitions to the incident wave field, a strategy conceptually related to the multi-segment floaters examined in [19].

Top-Shaped Buoy 2. A spinning-top profile of 160 mm maximum diameter and 240 mm overall height, tapering to a 50 mm lower apex with a draft line 150 mm from the top. The geometry follows the self-stabilizing top-shaped concept of Azam et al. [19], [20], in which the conical underbody minimizes flow separation and promotes pitch stability at the expense of waterplane area.

Cylindrical–Spherical Buoy 3. A composite body consisting of a cylindrical upper section of 180 mm diameter and 90 mm height mounted on a spherical lower body of 210 mm diameter, with an overall height of 230 mm, a 3 mm wall thickness, and a 10 mm axial bore accommodating the guide shaft. The spherical underbody concentrates submerged volume deep below the waterline the same design rationale underlying the bulbous-bottomed buoys of Ahmed et al. [23] thereby maximizing displaced volume and hydrodynamic coupling for a given waterplane diameter.

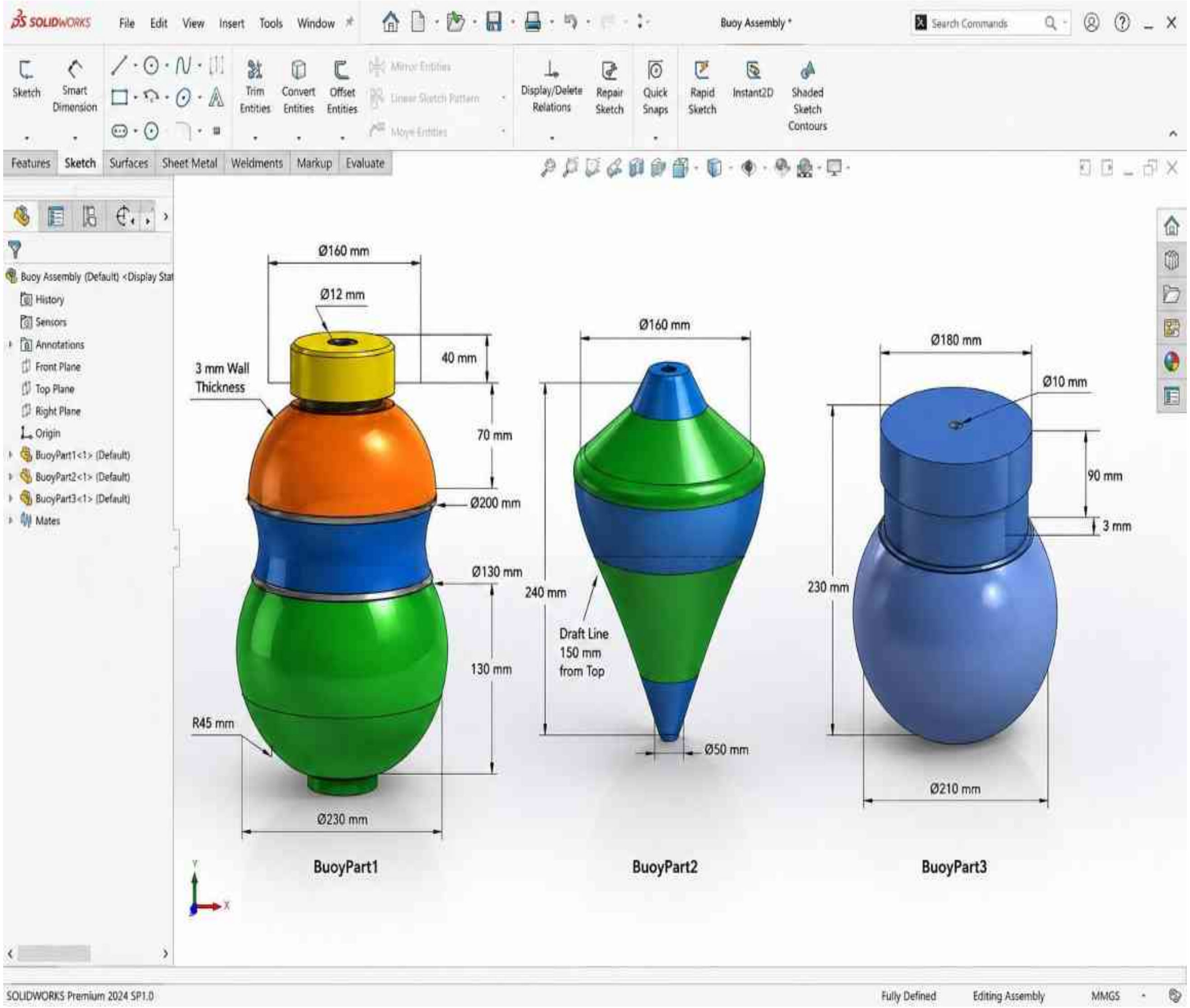

Figure 3: Three-Dimensional CAD models of the Buoy Geometries with Dimensions

All three models were assigned identical material properties, mass distributions consistent with their displaced volumes, and identical drafts relative to the mean water level, ensuring that the subsequent performance differences are attributable exclusively to geometric form.

2.2 Computational Domain

A three-dimensional numerical wave tank was constructed in ANSYS Fluent to resolve the viscous interaction between the incident flow and each buoy as in **Figure 4**. The rectangular domain was dimensioned to provide sufficient upstream fetch for wave development and adequate downstream length to suppress reflection contamination, with generous lateral and vertical clearances to minimize blockage effects. The buoy was positioned at the free surface near the longitudinal mid-station of the tank. The domain comprised stratified water and air regions, with the air–water interface captured by the volume-of-fluid (VOF) formulation.

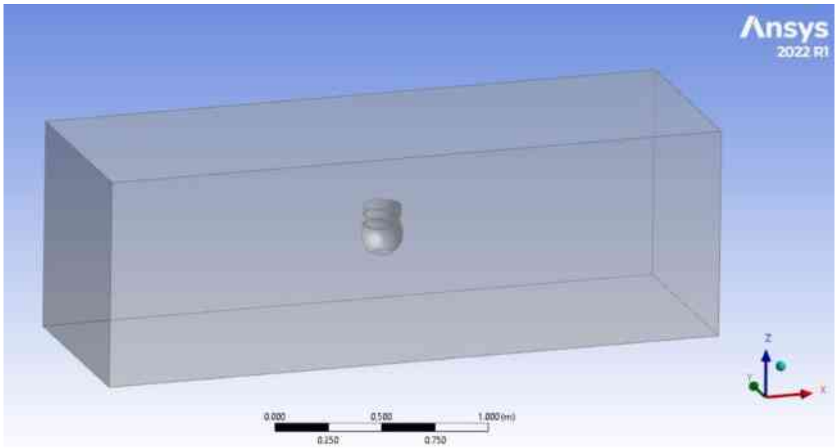

Figure 4: Wave Tank Computational Domain used for CFD Analysis in ANSYS Fluent

The inlet face introduced the prescribed wave/current condition (velocity inlet), the outlet face was assigned a pressure outlet permitting non-reflective outflow, and the remaining faces were treated as walls and symmetry planes as appropriate in **Figure 5**.

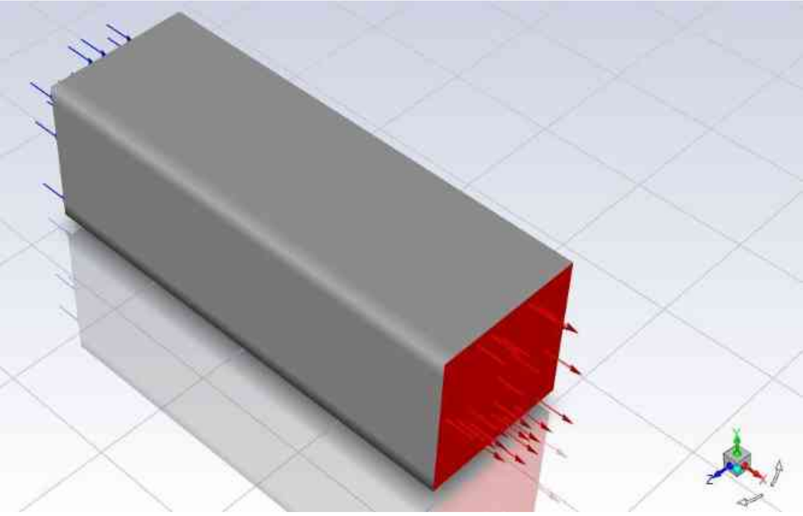

Figure 5: Boundary Conditions Applied to the Computational Domain

2.3 Mesh Generation

An unstructured mesh was generated with progressive refinement toward the buoy surface, where the steepest velocity and pressure gradients develop, and coarsening toward the far field to contain computational cost. For the AQWA panel models, a structured quadrilateral surface mesh was applied to the wetted geometry as shown in **Figure 6**.

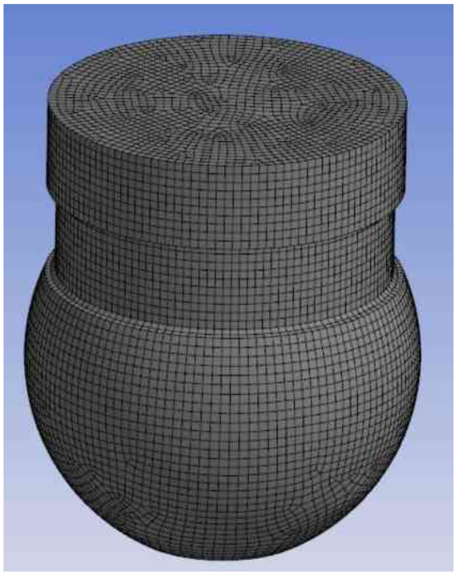

Figure 6: Mesh Generated on the Buoy Geometry

A formal mesh independence study was conducted for Buoy 3 using the heave RAO as the convergence metric (**Figure 7, Table 1**). Four panel densities were examined: 2500, 4500, 6500, and 8663 elements, producing heave RAO values of 3.82, 4.12, 4.28, and 4.35007 m/m, respectively. The relative change between the final two refinement levels fell below 2%, and further refinement to 12,000 elements produced negligible variation; the 8663-element mesh (8665 nodes) was therefore adopted for all production simulations. The asymptotic approach of the RAO toward 4.35 m/m confirms that the reported hydrodynamic coefficients are mesh-independent within engineering accuracy.

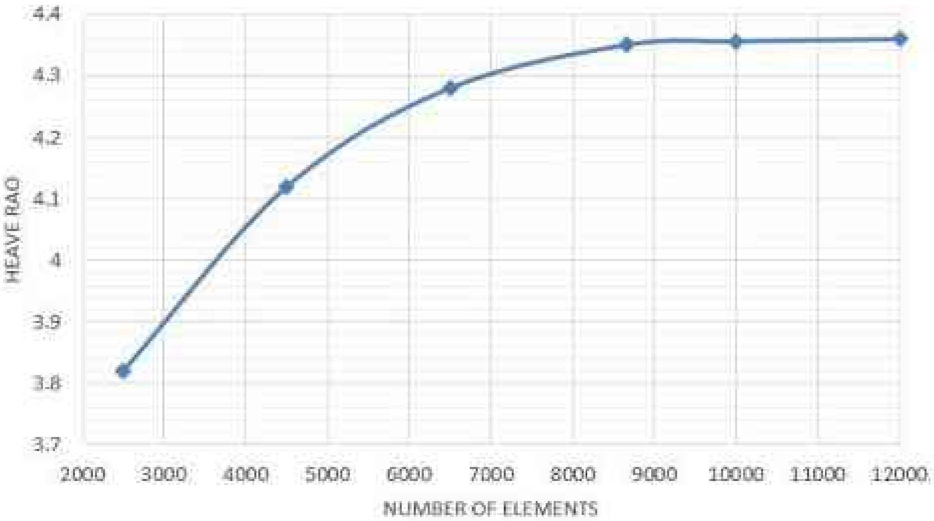

Figure 7: Mesh Convergence of Heave RAO with Element Count

Table 1: Mesh Convergence Study for Buoy 3

Mesh case	Elements	Heave RAO (m/m)	Change (%)
Coarse	2500	3.82	–
Medium	4500	4.12	+7.9
Fine	6500	4.28	+3.9
Final (AQWA)	8663	4.35	+1.6

2.4 CFD Solver Configuration

The transient CFD simulations employed a pressure-based solver with the VOF multiphase model resolving the free surface and the SST k–ω turbulence closure resolving near-wall and free-shear behavior a combination repeatedly validated for wave–structure interaction problems [27], [28]. Second-order discretization schemes were applied to the momentum equations, and convergence at each time step was enforced through scaled residual criteria. Identical solver settings, time-stepping, and boundary conditions were imposed for all three buoys to guarantee comparability.

2.5 Hydrodynamic Modeling Using ANSYS AQWA

Frequency-domain hydrodynamic analyses were performed in ANSYS AQWA, which solves the linearized potential-flow radiation/diffraction problem on the wetted body surface using the boundary element method [29], [30]. Each SolidWorks geometry was imported, positioned at its equilibrium draft, panelized, and assigned mass, center of gravity, and inertia properties consistent with its displacement. The analysis comprised two coupled stages as shown in **Figure 8** a hydrodynamic diffraction analysis defining wave directions and a frequency sweep extending to 37.39 rad/s from which the frequency-dependent added mass, radiation damping, excitation forces, and RAOs were extracted; and a hydrodynamic response analysis under a regular wave definition with non-heave degrees of freedom deactivated, consistent with the single-degree-of-freedom heave architecture of the proposed converter. Water density, gravitational acceleration, and mean water level corresponded to standard marine conditions, and identical environmental definitions were applied to all geometries.

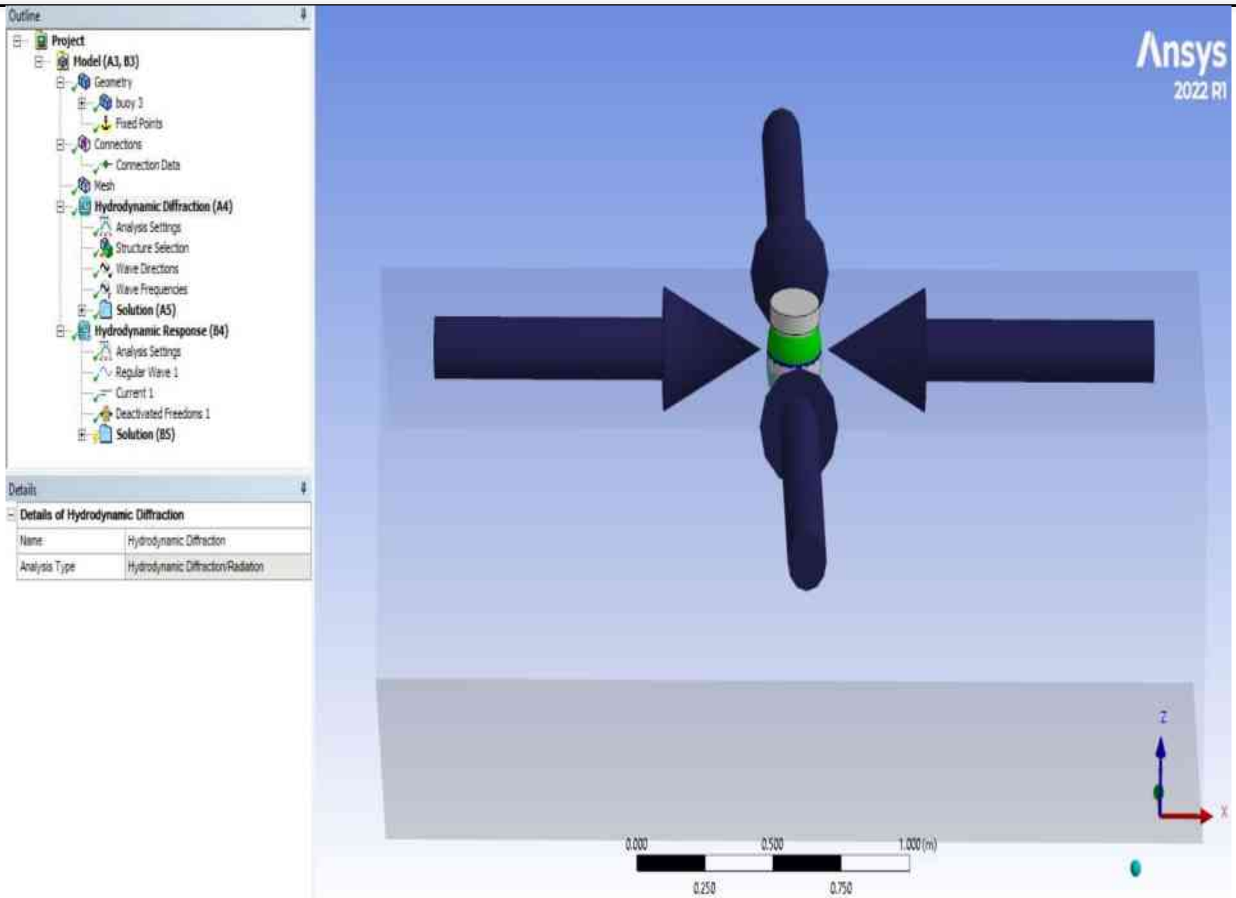

Details of Hydrodynamic Diffraction

Name	Hydrodynamic Diffraction
Analysis Type	Hydrodynamic Diffraction/Radiation

Figure 8: Frequency-Domain Analysis in ANSYS AQWA

2.6 Governing Equations

Under linear wave theory, the heave dynamics of a floating-point absorber are described by the frequency-domain equation of motion [31], [32]:

$$[m + a(\omega)]\,\ddot{z} + B(\omega)\,\dot{z} + C\,z = F_{ex}(\omega)\, e\text{^}(i\omega t) \tag{1}$$

where m is the structural mass, $a(\omega)$ the frequency-dependent added mass, $B(\omega)$ the radiation damping coefficient, $C = \rho g A_{vv}$ the hydrostatic restoring stiffness associated with the waterplane area A_{vv}, z the heave displacement, and F_{ex} the complex wave excitation force amplitude. The wave excitation force follows from integration of the incident and diffracted pressure fields over the instantaneous wetted surface S:

$$F_{ex} = -\iint_{s} p\, n_x\, dS, \quad p = -\rho\, \partial\varphi/\partial t \tag{2}$$

where φ is the total velocity potential and n_x the vertical component of the surface normal. The added mass and radiation damping arise from the real and imaginary parts of the radiation potential φ_r generated by unit-amplitude forced oscillation:

$$a(\omega) = Re\{(\rho/\check{z}) \iint_{s} (\partial\varphi_r/\partial t)\, n_x\, dS\}, \quad B(\omega) = Im\{(\rho\omega/\check{z}) \iint_{s} (\partial\varphi_r/\partial t)\, n_x\, dS\} \tag{3}$$

The non-dimensional heave response amplitude operator is defined as the ratio of heave amplitude Z to incident wave amplitude A:

$$RAO(\omega) = Z(\omega) / A \tag{4}$$

so that the heave displacement under a prescribed regular wave follows directly as:

$$Z = RAO \times A \tag{5}$$

and the corresponding heave velocity amplitude is:

$$v = \omega\, Z \tag{6}$$

The undamped heave natural frequency, which locates the RAO resonance peak, is:

$$\omega_n = \sqrt{(C / (m + a))} = \sqrt{(\rho g A_{vv} / (m + a))} \tag{7}$$

For a radiation-damping-dominated absorber, the time-averaged mechanical power extracted from the wave field is bounded by the radiated power and may be estimated as [31]:

$$P_m = \tfrac{1}{2} B v^2 \tag{8}$$

The deliverable electrical power accounts for the combined PTO and generator conversion efficiency η:

$$P_e = \eta P_m \tag{9}$$

For the geometrically scaled prototype, Froude similitude with scale factor $\lambda = L_p/L_m$ yields the transformation rules applied in Section 5:

$$Z_p = \lambda Z_m, \quad \omega_p = \omega_m/\sqrt{\lambda}, \quad B_p = B_m \lambda^3, \quad P \propto \lambda^{3.5} \tag{10}$$

3. Results and Discussion

3.1 Hydrostatic Characteristics

The hydrostatic computation establishes the first and arguably most consequential point of differentiation among the three geometries. Buoy 3 displaces 2.78×10^{-3} m³ at its equilibrium draft, exceeding Buoy 1 (1.90×10^{-3} m³) by 46% and Buoy 2 (5.26×10^{-4} m³) by a factor of 5.3. This ranking is a direct geometric consequence of how each profile distributes volume below the waterline. The spherical underbody of Buoy 3 places its volumetric centroid deep and concentrates the displaced fluid in a compact, hydrodynamically "full" form; the stepped profile of Buoy 1 sheds volume at each diameter reduction; and the conical taper of Buoy 2 although beneficial for pitch stability [20] sacrifices submerged volume aggressively toward the apex.

The physical significance of displaced volume in point absorber design cannot be overstated. In the long-wave (point absorber) regime, the heave excitation force scales to leading order with the dynamic pressure integrated over the wetted surface, which itself grows with submerged volume and waterplane area (Eq. (2)). A larger displacement therefore simultaneously raises the available excitation force and the hydrostatic stiffness, shifting the resonance characteristics into a usable band while increasing the energy flux intercepted from the wave field [23], [24]. On hydrostatic grounds alone, Buoy 3 enters the dynamic analysis with a decisive structural advantage.

3.2 CFD Flow Field Assessment

Before the frequency-domain comparison, the transient VOF simulations were interrogated to verify that all three buoys exhibit stable, well-behaved near-field flow. The velocity contours in **Figure 9** shows an essentially uniform incident stream that accelerates locally around each buoy as the flow contracts past the body, with a moderate wake forming downstream. Peak velocities of 1.652, 1.676, and 1.687 m/s were recorded for Buoys 1, 2, and 3, respectively a spread of barely 2%. The marginally higher peak for Buoy 3 reflects the stronger streamline curvature imposed by its full spherical underbody, but no geometry exhibits separation pathologies, excessive wake unsteadiness, or free-surface breakdown.

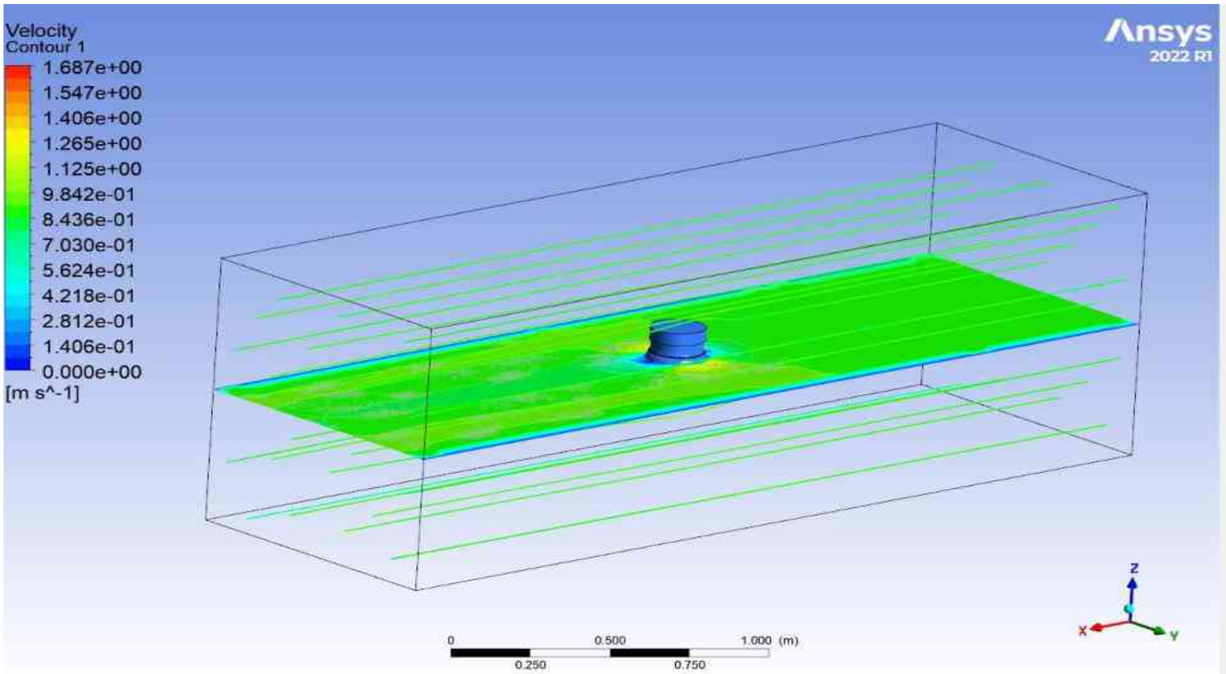

Figure 9: Velocity Contours and Streamlines Around the Optimized Buoy Geometry

The pressure contours as shown in **Figure 10** reproduce the same picture in the loading domain: stagnation-elevated pressure on the wave-facing region decays smoothly to a suction zone leeward of each body, with maxima of 14,685, 14,654, and 14,689 Pa for Buoys 1, 2, and 3 variations of less than 0.3%. The near-identity of these viscous loading metrics carries an important methodological implication that echoes the observations of Berenjkoob et al. [28]: steady near-field CFD diagnostics are insensitive discriminators of point absorber geometry, because the quantities that govern energy extraction radiative coupling, resonance placement, and frequency-dependent excitation are inherently oscillatory and cannot be inferred from instantaneous flow contours. The CFD stage thus serves its proper role of confirming hydrodynamic admissibility of all three candidates, while the performance discrimination is deferred to the frequency-domain analysis.

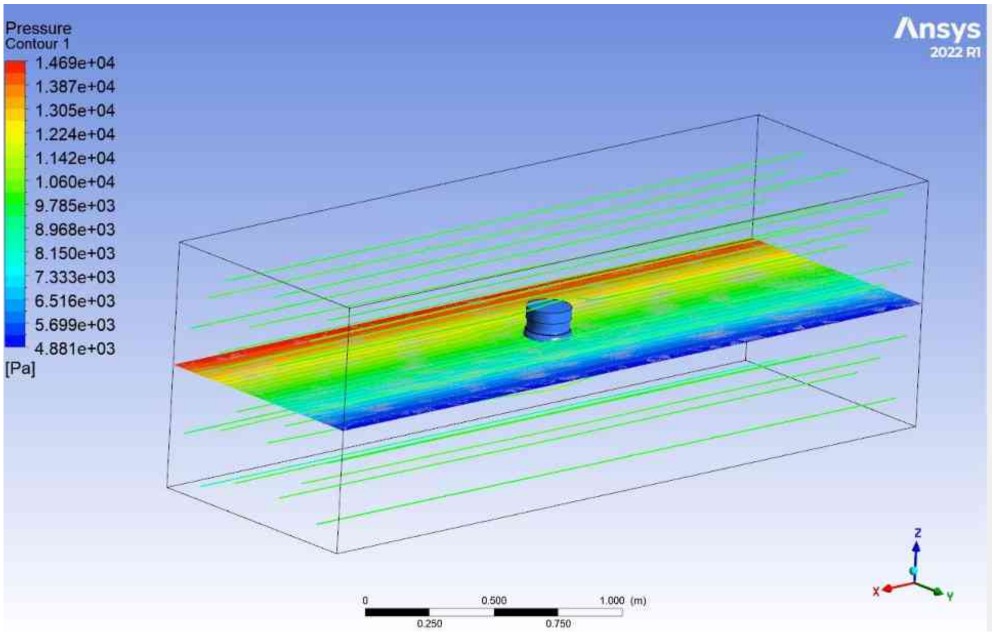

Figure 10: Pressure Contours Around the Optimized Buoy Geometry

3.3 Added Mass Analysis

The added mass responses as shown in **Figure 11** expose the first major dynamic separation among the geometries. Buoy 3 attains a peak added mass of 2.31 kg at 7.62 rad/s, against 1.83 kg at 8.47 rad/s for Buoy 1 and only 0.47 kg at 9.36 rad/s for Buoy 2, a 4.9-fold spread between the strongest and weakest configurations.

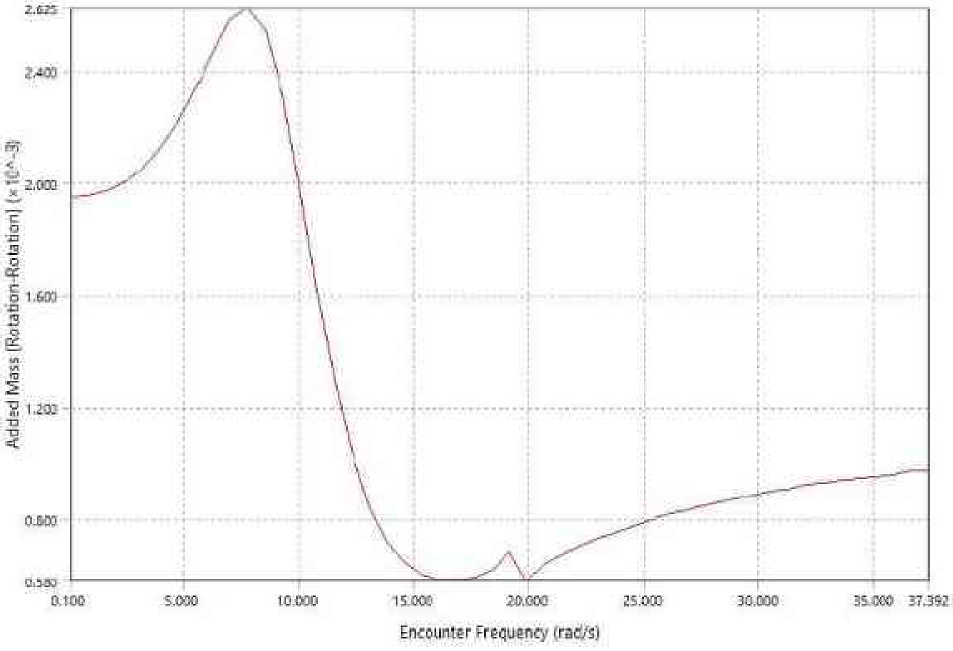

Figure 11: Variation of Added Mass with Encounter Frequency for the Optimized Buoy

The physics underlying this ranking follows directly from the radiation problem (Eq. (3)). Added mass quantifies the fluid inertia entrained by the oscillating body: a buoy whose submerged surface is large, deep, and bluff must accelerate a correspondingly large annulus of surrounding water with every heave cycle. The spherical underbody of Buoy 3 presents precisely such a surface its volumetric fullness below the waterline maximizes the entrained fluid mass whereas the slender cone of Buoy 2 slices through the fluid with minimal vertical blockage, entraining little surrounding water. The frequency at which each peak occurs is equally informative: the migration of the added mass maximum to lower frequency for Buoy 3 (7.62 rad/s) indicates that its radiation field interacts with longer, more energetic wave components, while the post-peak dip and recovery visible near 17–20 rad/s is the classical free-surface memory effect associated with standing-wave-type interference in the radiated field [31].

From an energy extraction standpoint, elevated added mass is doubly beneficial. First, through Eq. (7) it lowers the natural frequency, tuning the device toward the longer-period waves where ocean energy is concentrated. Second, it signifies strong hydrodynamic coupling a large fraction of the local wave field participates in the buoy's motion, which is the kinematic precondition for large energy transfer to the PTO [17], [33]. The weak coupling of Buoy 2 implies that, regardless of its motion amplitude, only a small mass of fluid exchanges energy with the body each cycle.

3.4 Radiation Damping Analysis

Radiation damping is the single most consequential coefficient for an absorber whose extractable power is governed by Eq. (8), and here the separation between geometries is starkest as in **Figure 12**. Buoy 3 reaches a peak radiation damping of 17.57 N/(m/s) at 11.72 rad/s; Buoy 1 peaks at 12.31 N/(m/s) at 12.06 rad/s; and Buoy 2 manages only 2.72 N/(m/s) at 15.53 rad/s. a factor of 6.5 below Buoy 3.

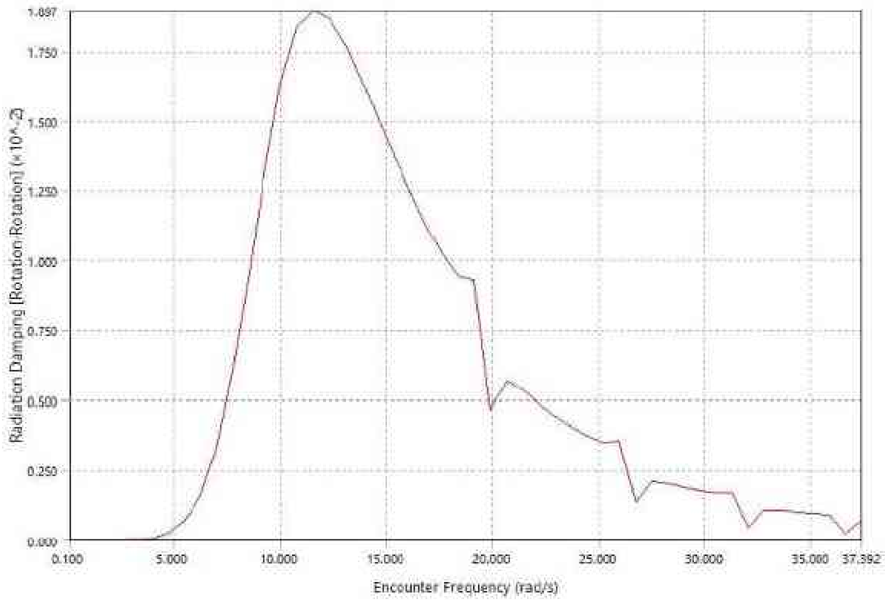

Figure 12: Variation of Radiation Damping with Encounter Frequency for the Optimized Buoy

Radiation damping measures the rate at which an oscillating body pumps energy into outgoing surface waves. By the reciprocity relations of linear wave theory, a body that radiates efficiently when forced is precisely the body that absorbs efficiently when excited radiation and absorption are two faces of the same wave-making capacity [31], [34]. The broad, energetic damping peak of Buoy 3 therefore certifies it as a strong two-way energy gateway: its full spherical hull displaces a large free-surface footprint per unit heave velocity, generating vigorous radiated waves and, conversely, drawing energy efficiently from incident ones. The narrow, weak response of Buoy 2 reveals the opposite its tapered form is nearly "wave-transparent," oscillating with minimal disturbance of the free surface and hence minimal capacity to exchange energy with the wave field. The bell-shaped decay of all curves beyond ~15 rad/s, punctuated by the irregular oscillation's characteristic of panel-method solutions at high frequency, reflects the diminishing radiation efficiency as wavelengths shrink relative to body dimensions.

It is emphasized that high radiation damping is desirable here precisely because the PTO extracts energy through the damped motion channel: optimal absorption occurs when PTO damping is matched to radiation damping, and a larger radiative coefficient raises the absolute power ceiling available for extraction [24], [35].

3.5 Wave Excitation Forces

The excitation force ranking mirrors the hydrostatic one, as anticipated by Eq. (2). With the largest displaced volume (2.78×10^{-3} m^3) and the fullest pressure-collecting underbody, Buoy 3 experiences the greatest wave excitation loading among the three candidates; Buoy 1 (1.90×10^{-3} m^3) follows, and Buoy 2 (5.26×10^{-4} m^3) trails substantially. The mechanism is geometric: the heave excitation force is the vertical resultant of the incident-plus-diffracted pressure field acting on the wetted surface, and a deep, voluminous hull simply intercepts more of the wave-induced dynamic pressure than a slender cone. Since the excitation force constitutes the sole energy input to the converter (Eq. (1)), the superior loading of Buoy 3 directly enlarges the energy budget available for conversion an observation consistent with the volume-sensitivity findings of hydrodynamic optimization studies on point absorbers [36], [37].

3.6 Response Amplitude Operators (RAOs)

The heave RAO curves shown in **Figure 13** introduce the one performance dimension in which Buoy 3 does not lead. Buoy 1 produces the tallest resonance peak, 5.66 m/m at 6.08 rad/s; Buoy 3 follows with 4.65 m/m at 6.25 rad/s (converging to 4.35 m/m on the final production mesh); and Buoy 2 exhibits the weakest response across the band. All three curves display the canonical point absorber signature a low-frequency asymptote near unity (wave-following behavior), a sharp resonance where excitation frequency meets the natural frequency of Eq. (7), and rapid roll-off at high frequency as body inertia decouples the buoy from short waves.

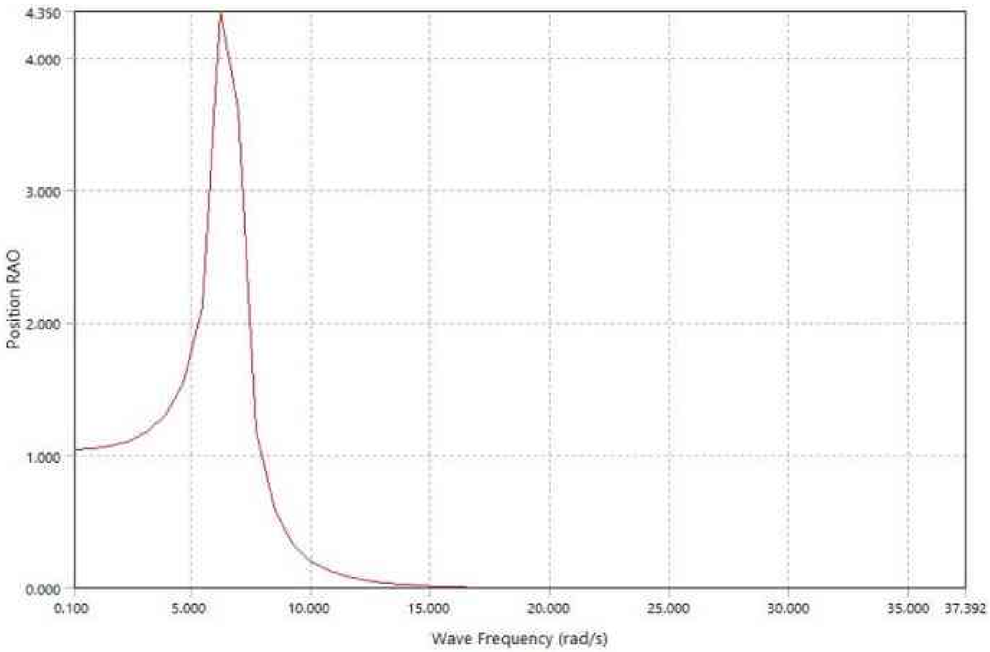

Figure 13: Heave Response Amplitude Operator of the Optimized Buoy Geometry

The physical explanation for the RAO inversion between Buoys 1 and 3 lies in the denominator of the steady-state response: heave amplitude at resonance is limited by total system damping. Buoy 1, with its moderate radiation damping (12.31 N/(m/s)), oscillates relatively unopposed and accumulates a taller resonance peak; Buoy 3, radiating far more vigorously (17.57 N/(m/s)), self-limits its motion by continuously shedding energy into the radiated wave field. The taller RAO of Buoy 1 is therefore not a sign of superior energy capture it is, in part, a sign of weaker energy exchange. This distinction is central to the selection logic developed below and aligns with the caution expressed in [18], [24] against motion-amplitude-based design criteria.

3.7 Heave Response

Translating the RAOs into dimensional motion under the design wave (A = 0.025 m, ω = 7.854 rad/s) by Eq. (5), Buoy 1 develops the largest vertical excursions, with Buoy 3 close behind ($Z = 4.35 \times 0.025 = 0.109$ m on the converged mesh). For a rack-and-pinion PTO, the heave stroke determines rack travel, and the heave velocity (Eq. (6)) determines pinion speed; both buoys deliver strokes comfortably within the mechanical operating envelope. The decisive question which buoy converts its motion into extractable power most effectively is resolved by the comparative assessment that follows.

3.8 Comparative Performance Assessment and Optimal Buoy Selection

Table 2 consolidates the complete performance matrix.

Table 2: Comparative Hydrodynamic Performance of the Three Buoy Geometries

Parameter	Buoy 1	Buoy 2	Buoy 3
Maximum CFD velocity (m/s)	1.65	1.68	1.69
Maximum CFD pressure (Pa)	14,685	14,654	14,689
Peak added mass (kg)	1.83	0.47	2.31
Added mass peak frequency (rad/s)	8.47	9.36	7.62
Peak radiation damping (N/(m/s))	12.31	2.72	17.57
Damping peak frequency (rad/s)	12.06	15.53	11.72
Peak heave RAO (m/m)	5.66	lowest	4.65
RAO peak frequency (rad/s)	6.08	–	6.25
Displaced volume (m³)	1.90×10^{-3}	5.26×10^{-4}	2.78×10^{-3}

The selection logic proceeds from the energy conversion chain rather than from any single coefficient. For a PTO-coupled absorber, the extractable power (Eq. (8)) is the product of the damping coefficient and the square of heave velocity; a buoy must therefore combine adequate motion with strong radiative coupling. Buoy 2 is eliminated immediately: deficient in volume, excitation, added mass, damping, and RAO alike, its slender profile renders it nearly transparent to the wave field. The genuine contest is between Buoy 1 the motion champion and Buoy 3 the coupling champion.

Buoy 3 prevails on four convergent grounds. First, its radiation damping exceeds that of Buoy 1 by 43%, directly raising the power ceiling of Eq. (8) for comparable velocity. Second, its added mass advantage (2.31 vs. 1.83 kg) signifies stronger fluid entrainment and tunes its resonance toward longer, more energetic waves. Third, its 46% larger displaced volume delivers proportionally greater excitation forcing the raw energy input to the system. Fourth, its RAO deficit relative to Buoy 1 (4.65 vs. 5.66 m/m) is modest and is itself the by-product of the very radiative vigor that makes it the better absorber: Buoy 1 moves more because it exchanges less. When the coefficients are combined through the absorption model, the **Table *3*.**

moderate motion of Buoy 3 acting against its superior damping extracts more power than the larger motion of Buoy 1 acting against weaker damping. Buoy 3 the cylindrical–spherical configuration is accordingly selected as the optimized geometry, a conclusion consonant with the bulbous-underbody findings of [16] and with the general principle that absorption, not amplitude, is the proper objective function for PA-WEC design [11], [24].

3.9 Power Absorption Capability of the Optimized Buoy

The power generation potential of Buoy 3 was quantified under the design regular wave ($A = 0.025$ m, $\omega = 7.854$ rad/s) using the converged hydrodynamic coefficients. The heave displacement follows from Eq. (5) as $Z = 4.35 \times 0.025 = 0.109$ m, and the heave velocity from Eq. (6) as $v = 7.854 \times 0.109 = 0.854$ m/s ≈ 0.85 m/s. With $B = 17.57$ N/(m/s), the mechanical power absorbed (Eq. (8)) is $P_m = ½ \times 17.57 \times (0.854)^2 = 6.40$ W, and assuming a combined rack-and-pinion and generator efficiency of $\eta = 0.80$, the electrical output (Eq. (9)) is $P_e = 0.80 \times 6.40 = 5.12$ W. The complete calculation chain is summarized in

Table 3: Estimated Power Generation Performance of the Optimized Buoy 3

Parameter	Value
Wave amplitude, A	0.025 m
Wave frequency, ω	7.854 rad/s
Heave RAO (converged)	4.35 m/m
Heave displacement, Z	0.109 m
Heave velocity, v	0.85 m/s
Radiation damping, B	17.57 N/(m/s)
Mechanical power, P_m	6.40 W
Theoretical electrical power, P_e	5.12 W

The result merits physical interpretation. The 0.109 m stroke more than four wave amplitudes confirm operation in the near-resonant regime where point absorbers realize their characteristic capture-width amplification. The quadratic dependence of P_m on velocity explains why the frequency placement of the damping and RAO peaks matters as much as their magnitudes: Buoy 3's coefficients remain elevated in the band surrounding the design frequency, sustaining absorption away from the exact resonance point. An output of order 5 W at laboratory scale is consistent with the small-scale point absorber estimates reported for comparable buoy dimensions and wave climates [19], [38], and positions the device appropriately for low-power offshore applications sensor buoys, navigation lights, and monitoring platforms pending the favorable $\lambda^{3.5}$ scaling discussed in Section 5.

4. Experimental Validation

4.1 Prototype Fabrication

To verify the operational feasibility of the optimized configuration, a laboratory-scale prototype of Buoy 3 was fabricated. The optimized geometry selected for fabrication is shown in **Figure 14**. The buoy was produced from lightweight material to preserve the buoyancy ratio, and particular care was taken to reproduce the cylindrical–spherical profile faithfully, since geometric similarity is the prerequisite for meaningful Froude-scaled comparison between numerical and experimental responses.

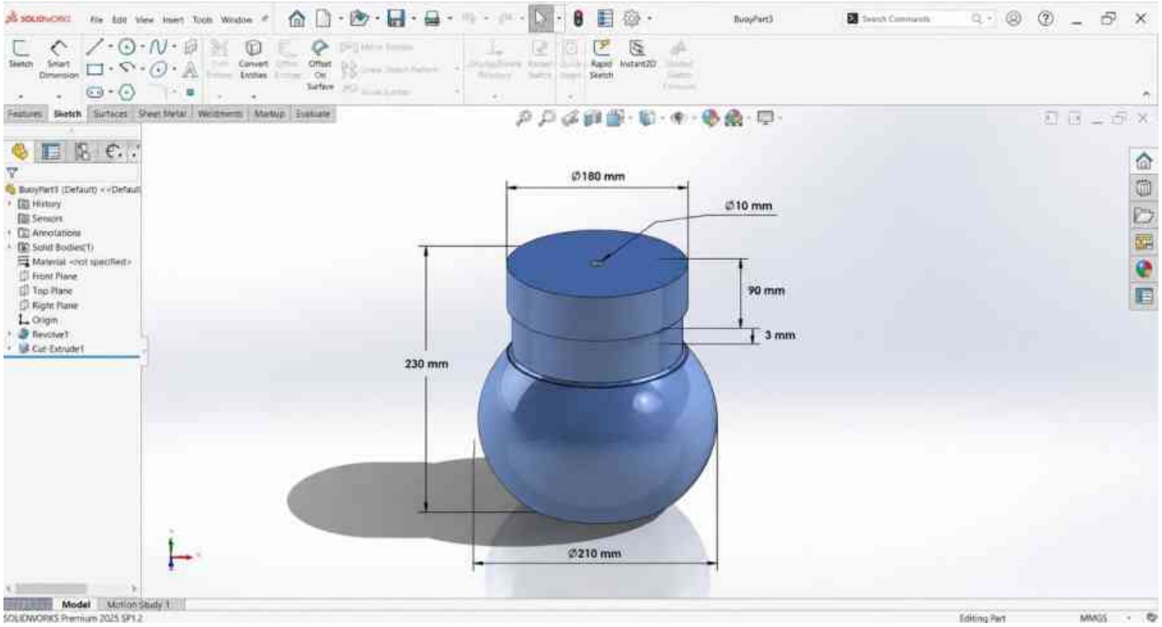

Figure 14: Optimized Cylindrical–Spherical Buoy Geometry Selected for Prototype Fabrication

Manufacturing and flume constraints dictated a reduced-scale model of 132 mm height and 120 mm maximum diameter, corresponding to a geometric scale factor λ = 132/230 = 0.574 relative to the numerical model as in **Table 4**.

Table 4: Principal Dimensions of the Optimized Buoy and Fabricated Prototype

Parameter	Numerical model	Fabricated prototype
Height (mm)	230	132
Maximum diameter (mm)	206	120
Scale factor, λ	1.00	0.574

4.2 Rack-and-Pinion Power Take-Off

The vertical buoy oscillation was converted to rotation through a rack-and-pinion PTO as shown in **Figure 15**. The rack was rigidly attached to the buoy support shaft, which translates vertically within an aluminum guide rail assembly that constrains motion to pure heave, suppresses lateral play, and minimizes frictional misalignment losses. A pinion gear on a supported rotating shaft remained in continuous mesh with the rack throughout the oscillation cycle.

Figure 15: Rack-and-Pinion Power Take-off Mechanism with Aluminum Guide Rail Assembly

Rack-and-pinion conversion was selected for its mechanical directness, fabrication simplicity, and proven reliability in oscillating-body energy converters [39], [40]. The assembled PTO column mounted on the wave tank is shown in **Figure 16**.

Figure 16: Assembled Power Take-off Column and Guide System Mounted on the Acrylic Wave Tank

4.3 Electrical Generation and Instrumentation

A 130-size permanent-magnet DC motor, operated as a generator, was coupled directly to the pinion shaft as shown in **Figure 17**. The generated voltage was measured across the generator terminals with a digital multimeter; readings were logged continuously during wave excitation, together with observations of buoy kinematics, rack engagement, and structural stability.

Figure 17: Generator and Electrical Measurement Arrangement of the Fabricated Prototype

4.4 Wave Flume Testing

Experiments were conducted in a custom-fabricated transparent acrylic wave tank of 914 mm × 457 mm × 610 mm (**Figure 18**, Table 5), whose transparency permitted direct observation of buoy motion, free-surface behavior, and PTO operation. The buoy was positioned centrally with adequate wall clearance to limit reflection interference, partially submerged to its design draft, and excited by manually generated regular waves. The procedure comprised: filling the tank to the operating level; installing the buoy in the guide assembly; engaging the rack-and-pinion; coupling the generator and instrumentation; generating regular waves; and recording voltage output over repeated runs to confirm repeatability.

Figure 18: Acrylic Wave Tank used for Experimental Testing of the Fabricated Wave Energy Converter

Table 5. Acrylic Wave Tank Specifications.

Parameter	Value
Length	914 mm
Width	457 mm
Height	610 mm
Material	Acrylic
Wave type	Regular laboratory waves

4.5 Experimental Results

Under manual regular-wave excitation, the prototype converted heave motion into continuous generator rotation and produced measurable electrical output throughout testing, with terminal voltages ranging from approximately 0.27 V to a peak of 1.50 V depending on wave amplitude and excitation regularity. The system operated without rack disengagement, binding, or structural instability across repeated runs. The successful and repeatable conversion of wave-induced motion into electricity constitutes direct experimental confirmation of the converter concept; the quantitative relationship between this output and the 5.12 W numerical prediction is established through the scaling analysis of Section 5.

5. Discussion of Scaling Effects

5.1 Froude-Scaled Hydrodynamics of the Prototype

The prototype response was reconciled with the numerical model through the Froude similitude relations of Eq. (10), with $\lambda = 0.574$. The heave displacement scales as $Z_p = \lambda Z_m = 0.574 \times 0.109 = 0.063$ m; the wave frequency as $\omega_p = \omega_m/\sqrt{\lambda} = 7.854/\sqrt{0.574} = 10.37$ rad/s; and the heave velocity as $v_p = \omega_p Z_p = 10.37 \times 0.063 = 0.653$ m/s. The radiation damping transforms with the cube of the length scale, $B_p = 17.57 \times (0.574)^3 = 3.32$

N/(m/s). Substituting into Eq. (8), the scaled mechanical power is $P_m = \frac{1}{2} \times 3.32 \times (0.653)^2 = 0.71$ W, and with $\eta = 0.80$ the scaled electrical output (Eq. (9)) is $P_e = 0.57$ W.

5.2 Power Scaling Law

The aggregate effect of geometric reduction on absorbed power follows the classical Froude exponent, $P \propto \lambda^{3.5}$. Substituting the prototype scale factor gives $P_{scale} = (0.58)^{3.5} \approx 0.15$, so that the fabricated prototype can theoretically deliver only ~15% of the full-model output: $P_{proto} = 5.14 \times 0.15 \approx 0.77$ W. The two independent estimates 0.57 W from coefficient-by-coefficient Froude transformation and 0.77 W from the $\lambda^{3.5}$ power law bracket a consistent sub-watt expectation for the laboratory device, an order of magnitude below the full numerical model purely on geometric grounds.

5.3 Reconciliation of Numerical and Experimental Results

The measured peak voltage of 1.50 V from the 130-size generator corresponds to a sub-watt electrical output, in agreement with the scaled predictions. The residual gap between the theoretical scaled power (0.57–0.77 W) and the realized output is attributable to loss mechanisms that lie outside the inviscid numerical framework and that disproportionately penalize small-scale devices: (1) mechanical transmission losses sliding friction in the guide rails, gear-mesh friction and backlash in the rack-and-pinion, and bearing resistance, which consume a fixed torque overhead that is proportionally severe at sub-watt power levels; (2) generator inefficiency miniature DC machines operate well below the assumed 80% conversion efficiency at the low rotational speeds produced by laboratory waves, with cogging torque and winding resistance dominating; (3) imperfect wave excitation manually generated waves deviate from the monochromatic regular waves of the frequency-domain analysis in amplitude regularity and spectral purity, displacing the operating point from resonance; (4) flume boundary effects wall and end-wall reflections in the compact tank superpose parasitic components on the incident field; and (5) viscous and scale effects Reynolds-number dissimilarity under Froude scaling exaggerates viscous damping at model scale, a well-documented bias in small WEC experiments [41], [42].

Crucially, the ordering of these results validates the numerical framework: the experiment was designed as a proof-of-concept demonstration, and the measured output falls precisely within the band that Froude scaling predicts from the AQWA coefficients. The agreement between the scaling-law estimate and the observed performance confirms that the discrepancy between the 5.12 W full-model prediction and the laboratory measurement is dominated by geometric scale not by error in the hydrodynamic model and supports confident extrapolation of the optimized geometry toward larger deployments, where the $\lambda^{3.5}$ law operates in the favourable direction.

6. Conclusions

This study presented a unified CFD and frequency-domain hydrodynamic optimization of three-point absorber buoy geometries, followed by power estimation, prototype fabrication, and experimental validation of the optimal configuration. The principal conclusions are as follows:

(1) **Near-field CFD metrics do not discriminate buoy geometry.** Peak velocities (1.65–1.69 m/s) and pressures (14.65–14.69 kPa) differed by less than 2% and 0.3% across the three buoys, confirming hydrodynamic admissibility of all candidates while demonstrating that geometric selection must rest on frequency-domain radiation/diffraction coefficients.

(2) **Buoy geometry governs radiative coupling decisively.** The cylindrical–spherical buoy (Buoy 3) achieved a peak added mass of 2.31 kg and peak radiation damping of 17.57 N/(m/s) respectively 26% and 43% above the multi-section buoy, and 4.9× and 6.5× above the top-shaped buoy together with the largest displaced volume (2.78×10^{-3} m^3, +46% over Buoy 1). The spherical underbody's concentration of submerged volume is identified as the geometric mechanism maximizing fluid entrainment, wave-making capacity, and excitation loading.

(3) **Motion amplitude is an unreliable selection criterion.** Although the multi-section buoy produced the tallest heave RAO (5.66 m/m at 6.08 rad/s versus 4.65 m/m at 6.25 rad/s for Buoy 3), its larger motion reflects weaker radiative energy exchange rather than superior capture. When the coefficients are propagated through the absorption model, the strongly coupled Buoy 3 extracts more power, establishing absorption capacity not RAO as the proper objective function for PTO-based converters.

(4) **The optimized buoy delivers meaningful small-scale power.** Under a regular wave of 0.025 m amplitude and 7.854 rad/s, Buoy 3 attains a heave stroke of 0.109 m and velocity of 0.85 m/s, absorbing 6.40 W of mechanical power and yielding a theoretical electrical output of 5.12 W at 80% conversion efficiency sufficient for offshore sensing, navigation, and monitoring applications.

(5) **Experimental validation confirms the concept and the scaling framework.** A 0.574-scale prototype with a rack-and-pinion PTO and 130-size DC generator produced repeatable voltages of 0.27–1.50 V in a 914 × 457 × 610 mm acrylic flume. Froude-scaled predictions (0.57 W by coefficient transformation; 0.77 W by the $P \propto \lambda^{3.5}$ law, i.e. ~15% of full-model output) bracket the observed performance, demonstrating that the numerical–experimental gap is governed by geometric scale and quantifiable mechanical/electrical losses rather than hydrodynamic modeling error.

(6) **Engineering significance.** The combined dual-framework methodology viscous CFD screening, BEM coefficient extraction, absorption-based selection, and scaling-reconciled validation constitutes a transferable design pipeline for point absorber development, and the favourable $\lambda^{3.5}$ power scaling indicates substantial output growth for the cylindrical–spherical geometry at deployment scale.

Future work should address larger-scale prototypes to suppress Froude–Reynolds bias, bidirectional and higher-efficiency PTO architectures, simultaneous voltage–current instrumentation for direct power measurement, irregular-wave and real-sea testing, and multi-objective shape optimization building on the cylindrical–spherical baseline established here.

REFERENCES

[1] R. Pelc and R. M. Fujita, “Renewable energy from the ocean,” *Marine Policy*, vol. 26, no. 6, pp. 471–479, 2002.

[2] T. Aderinto and H. Li, “Review on power performance and efficiency of wave energy converters,” *Energies*, vol. 12, p. 4329, 2019.

[3] K. Gunn and C. Stock-Williams, “Quantifying the global wave power resource,” *Renewable Energy*, vol. 44, pp. 296–304, 2012.

[4] C. Zheng, X. Pan, and J. Liu, “Global ocean wave energy resource assessment with the Maritime Silk Road as a case study,” *Renewable Energy*, vol. 169, pp. 843–854, 2020.

[5] J. Goggins and W. Finnegan, “Shape optimization of floating wave energy converters for a specified sea state,” *Renewable Energy*, vol. 71, pp. 208–220, 2014.

[6] M. M. Ahsan, M. Zulqernain, H. Ahmad, B. A. Wajid, S. Shahzad, and M. Hussain, “Reducing the Operational Energy Consumption in Buildings by Passive Cooling Techniques Using Building Information Modelling Tools,” *International Journal of Renewable Energy Research*, vol. 9, no. 1, pp. 343–353, 2019.

[7] B. A. Wajid *et al.*, “Energy Performance Evaluation and Retrofitting Strategies for Sustainable Hostel Buildings in Pakistan,” *QUEST Research Journal*, vol. 23, no. 1, pp. 8–29, 2025.

[8] M. M. Ahsan, W. Cheng, A. B. Hussain, X. Chen, and B. A. Wajid, “Knowledge Mapping of Research Progress in Vertical Greenery Systems (VGS) from 2000 to 2021 Using CiteSpace Based Scientometric Analysis,” *Energy and Buildings*, vol. 256, p. 111768, 2022.

[9] A. Ahmed *et al.*, “Additively Manufactured Nano-Mechanical Energy Harvesting Systems: Advancements, Potential Applications, Challenges and Future Perspectives,” *Nano Convergence*, vol. 8, no. 37, 2021, doi: 10.1186/s40580-021-00289-0.

[10] W. Cheng, D. Blamaud, Y. Chu, L. Meng, J. Lu, and W. A. Basit, “Transfer Path Analysis and Contribution Evaluation Using SVD- and PCA-Based Operational Transfer Path Analysis,” *Shock and Vibration*, vol. 2020, p. 9673838, 2020, doi: 10.1155/2020/9673838.

[11] W. Cheng *et al.*, “A Customized Scheme of Crosstalk Cancellation for Operational Transfer Path Analysis and Experimental Validation,” *Journal of Sound and Vibration*, vol. 515, p. 116506, 2021, doi: 10.1016/j.jsv.2021.116506.

[12] A. Azam *et al.*, “Design, Fabrication and Implementation of HE-OBCU-EGR Emission Control Unit on CI Engine and Analysis of Its Effects on Regulated Gaseous Engine Emissions,” *Journal of King Saud University – Engineering Sciences*, vol. 33, no. 1, pp. 61–69, 2021, doi: 10.1016/j.jksues.2019.10.002.

[13] P. Contestabile, D. Vicinanza, F. Ferrante, and E. Di Ferraro, “Wave energy technologies: State-of-the-art and future perspectives,” *Renewable and Sustainable Energy Reviews*, vol. 72, pp. 149–169, 2017.

[14] D. Curto, S. Franzitta, M. Guercio, and A. P. Brucato, “Wave energy conversion technologies: A review of current status and future perspectives,” *Renewable and Sustainable Energy Reviews*, vol. 125, p. 109817, 2020.

[15] R. P. F. Gomes, C. Henriques, L. M. C. Gato, and A. F. O. Falcao, “Floating body wave energy converters: A review,” *Renewable and Sustainable Energy Reviews*, vol. 132, p. 110081, 2020.

[16] D. Khojasteh and R. Kamali, “Evaluation of wave energy absorption by heaving point absorber buoys at various points in regular and irregular wave conditions,” *Renewable Energy*, vol. 92, pp. 69–80, 2016.

[17] Y. Gao and L. Xiao, “Effects of buoy shape and harvester shape on wave energy extraction and output of a hydraulic conversion system,” *Applied Energy*, vol. 299, p. 117278, 2021.

[18] B. Guo and J. V. Ringwood, “Geometric optimization of wave energy conversion devices,” *Applied Energy*, vol. 299, p. 117100, 2021.

[19] A. Azam *et al.*, “Design and analysis of the optimal spinning top-shaped buoy for wave energy harvesting in low energy density seas for sustainable marine aquaculture,” *Ocean Engineering*, vol. 255, p. 111434, 2022.

[20] A. Azam *et al.*, “A self-stabilizing point absorber wave energy converter with a top-shaped buoy and nonlinear power take-off for oceanographic applications,” *Ocean Engineering*, vol. 288, p. 116018, 2023.

[21] A. Ahmed, Y. Wang, A. Azam, N. Li, C. Jia, and Z. Zhang, “Design of an S-shaped point-absorber wave energy converter with a non-linear PTO to power the satellite-respondent buoys in the East China Sea,” *Ocean Engineering*, vol. 275, p. 114162, 2023.

[22] A. Ahmed, A. Azam, Y. Wang, X. Tan, M. Yi, and Z. Zhang, “On the S-shaped floaters for a Wavestar-like wave energy converter with an I-shaped mechanical power take-off,” *Energy Conversion and Management: X*, vol. 19, p. 100387, 2023.

[23] A. Ahmed *et al.*, “An isomorphic Froude scaling approach to bulbous-bottomed buoys in wave energy converters for smart floating cities,” *Applied Ocean Research*, vol. 156, p. 104485, 2025.

[24] J. Pastor and Y. Liu, “Power absorption modeling and optimization of a point absorbing wave energy converter using numerical methods,” *Renewable Energy*, vol. 67, pp. 329–341, 2014.

[25] M. Shadman, S. F. Rodriguez, C. A. Nogueira, and I. C. M. Nogueira, "A geometrical optimization method applied to a heaving point absorber wave energy converter," *Renewable Energy*, vol. 115, pp. 335–346, 2018.

[26] A. Garcia-Teruel and D. Forehand, "A review of geometry optimisation of wave energy converters," *Renewable and Sustainable Energy Reviews*, vol. 139, p. 110593, 2021.

[27] S. Jin, R. Patton, R. Guo, and B. Li, "Enhancement of wave energy absorption efficiency via geometry and power take-off damping tuning," *Energy*, vol. 169, pp. 819–832, 2019.

[28] M. Berenjkoob, Y. Gao, and L. Xiao, "Influence of the shape of a buoy on the efficiency of its dual-motion wave energy conversion," *Renewable Energy*, vol. 214, p. 119898, 2021.

[29] A. Azam, A. Ahmed, A. Qammar, A. N. Shah, and Z. Zhang, "From model-scale to full-scale: Optimizing buoy geometry for enhanced energy conversion in PA-WECs," *Ocean Engineering*, 2025.

[30] B. Guo, Y. Gao, and L. Xiao, "Performance enhancement techniques for point absorber wave energy converters," *Renewable Energy*, vol. 186, pp. 1188–1205, 2022.

[31] J. Falnes and A. Kurniawan, *Ocean Waves and Oscillating Systems: Linear Interactions Including Wave-Energy Extraction*, 2nd ed. Cambridge, UK: Cambridge University Press, 2020.

[32] K. Budal and J. Falnes, "A resonant point absorber of ocean-wave power," *Nature*, vol. 256, no. 5517, pp. 478–479, 1975.

[33] X. Ji, A. A. Shami, J. Monty, and J. Wang, "Modelling of linear and non-linear two-body wave energy converter under regular and irregular wave conditions," *Renewable Energy*, vol. 147, pp. 487–501, 2020.

[34] A. Babarit, "A database of capture width ratio of wave energy converters," *Renewable Energy*, vol. 80, pp. 610–628, 2015.

[35] J. V. Ringwood, G. Bacelli, and F. Fusco, "Energy-maximizing control of wave-energy converters," *IEEE Control Systems Magazine*, vol. 34, no. 5, pp. 30–55, 2014.

[36] V. Piscopo and A. Scamardella, "A new optimization procedure of heaving point absorber wave energy converter," *Ocean Engineering*, vol. 116, pp. 212–225, 2016.

[37] J. D. N. Tom and V. Yim, "Hydrodynamic optimization of point absorber wave energy converters," *Renewable Energy*, vol. 123, pp. 499–512, 2018.

[38] S. Bozzi, A. Miquel, A. Antonini, J. Passoni, and M. Archetti, "Modeling of a point absorber wave energy converter for energy production assessment," *Renewable Energy*, vol. 116, pp. 539–546, 2018.

[39] C. Liang, A. Ji, and J. Luo, "Design, fabrication, simulation and testing of an ocean wave energy converter with mechanical motion rectifier," *Ocean Engineering*, vol. 136, pp. 190–200, 2017.

[40] X. Li *et al.*, "A compact mechanical power take-off for wave energy converters," *Energies*, vol. 13, p. 14549, 2020.

[41] J. Orphin, R. Nader, and I. Penesis, "Uncertainty analysis of a wave energy converter model test," *Ocean Engineering*, vol. 231, p. 109547, 2021.

[42] N. Fonseca, T. Soares, and M. Pascoal, "Experimental validation of the WEC-Sim tool for model ocean wave energy conversion," *Renewable Energy*, vol. 120, pp. 451–463, 2016.